

ARTICLE

Open Access

Single-cell RNA sequencing of subcutaneous adipose tissues identifies therapeutic targets for cancer-associated lymphedema

Xuanyu Liu¹, Meng Yuan¹, Qinqin Xiang², Zhujun Li³, Fen Xu¹, Wen Chen¹, Jie Chen³, Jiuzuo Huang³, Nanze Yu³, Zhou Zhou¹✉ and Xiao Long³✉

Abstract

Cancer-associated lymphedema frequently occurs following lymph node resection for cancer treatment. However, we still lack effective targeted medical therapies for the treatment or prevention of this complication. An in-depth elucidation of the cellular alterations in subcutaneous adipose tissues of lymphedema is essential for medical development. We performed single-cell RNA sequencing of 70,209 cells of the stromal vascular fraction of adipose tissues from lymphedema patients and healthy donors. Four subpopulations of adipose-derived stromal cells (ASCs) were identified. Among them, the *PRG4*⁺/*CLEC3B*⁺ ASC subpopulation c3 was significantly expanded in lymphedema and related to adipose tissue fibrosis. Knockdown of *CLEC3B* in vitro could significantly attenuate the fibrogenesis of ASCs from patients. Adipose tissues of lymphedema displayed a striking depletion of *LYVE*⁺ anti-inflammatory macrophages and exhibited a pro-inflammatory microenvironment. Pharmacological blockage of Trem1, an immune receptor predominantly expressed by the pro-inflammatory macrophages, using murine LR12, a dodecapeptide, could significantly alleviate lymphedema in a mouse tail model. Cell–cell communication analysis uncovered a perivascular ligand–receptor interaction module among ASCs, macrophages, and vascular endothelial cells. We provided a comprehensive analysis of the lineage–specific changes in the adipose tissues from lymphedema patients at a single-cell resolution. *CLEC3B* was found to be a potential target for alleviating adipose tissue fibrosis. Pharmacological blockage of TREM1 using LR12 could serve as a promising medical therapy for treating lymphedema.

Introduction

Lymphedema is defined by chronic tissue edema that results from lymphatic drainage disorders due to intrinsic fault (primary lymphedema) or damage (secondary

lymphedema) to the lymphatic system¹. Secondary lymphedema is the most prevalent form and frequently occurs following lymph node resection for cancer treatment, i.e., cancer-associated lymphedema². Up to 20% of women develop this condition following treatment for breast cancer³. Lymphedema is characterized by progressive swelling, chronic inflammation, excessive fibrosis, and adipose deposition in the affected limbs⁴. Lymphedema usually exerts a significant physical and psychological burden on cancer survivors and severely affects their quality of life; however, the clinical treatment remains palliative⁵. We still lack effective therapies, in particular, targeted medical therapies, for the treatment or prevention of this complication, which is partially due to the incomplete understanding of the cellular mechanisms underlying the pathogenesis.

Correspondence: Zhou Zhou (zhouzhou@fuwaihospital.org) or Xiao Long (pumclongxiao@126.com)

¹State Key Laboratory of Cardiovascular Disease, Beijing Key Laboratory for Molecular Diagnostics of Cardiovascular Diseases, Center of Laboratory Medicine, Fuwai Hospital, National Center for Cardiovascular Diseases, Chinese Academy of Medical Sciences and Peking Union Medical College, Beijing, China

²Prenatal Diagnosis Center, Department of Obstetrics and Gynecologic, Key Laboratory of Birth Defects and Related Diseases of Women and Children, Ministry of Education, West China Second University Hospital, Sichuan University, Chengdu, Sichuan, China

Full list of author information is available at the end of the article
These authors contributed equally: Xuanyu Liu, Meng Yuan

© The Author(s) 2022



Open Access This article is licensed under a Creative Commons Attribution 4.0 International License, which permits use, sharing, adaptation, distribution and reproduction in any medium or format, as long as you give appropriate credit to the original author(s) and the source, provide a link to the Creative Commons license, and indicate if changes were made. The images or other third party material in this article are included in the article's Creative Commons license, unless indicated otherwise in a credit line to the material. If material is not included in the article's Creative Commons license and your intended use is not permitted by statutory regulation or exceeds the permitted use, you will need to obtain permission directly from the copyright holder. To view a copy of this license, visit <http://creativecommons.org/licenses/by/4.0/>.

Adipose tissue is not simply a container of fat, but an endocrine organ, which is composed of multiple types of cells, such as adipose-derived stromal cells (ASCs), adipocytes, vascular cells (e.g., vascular endothelial cells and pericytes), and immune cells⁶. All nonadipocyte cells are known as the stromal vascular fraction (SVF), which can be isolated through enzymatic digestion⁷. Lymphatic fluid stasis in the limbs of patients with lymphedema will ultimately result in increased subcutaneous adipose tissue volume and excess adipose deposition, which may lead to further deterioration of the lymphatic system⁸. Previous studies have reported significant alterations in the SVF of subcutaneous adipose tissues in lymphedema concerning cellular composition, proliferation, and differentiation capacity, and these studies highlight the important role of the SVF alterations in the pathophysiology of lymphedema^{9–12}. However, previous studies generally relied on the expression of a limited number of markers and focused on a few cell lineages. We still lack a comprehensive and accurate understanding of the cellular and molecular alterations in subcutaneous adipose tissues of lymphedema.

Recent technical advances in single-cell RNA sequencing (scRNA-seq) have enabled the transcriptomes of tens of thousands of cells to be assayed at a single experiment¹³. Compared with bulk RNA-seq, scRNA-seq allows for unbiased cellular heterogeneity dissection at an unprecedented resolution¹⁴. scRNA-seq is emerging as a powerful tool for understanding the cellular and molecular mechanisms underlying the pathogenesis of diseases such as pulmonary fibrosis¹⁵ and lupus nephritis¹⁶. scRNA-seq has been applied to dissect the cellular heterogeneity of the SVF in mice^{17,18} and humans⁶ in healthy conditions. However, to our knowledge, few studies have been performed to explore the alterations in the SVF under a diseased condition, for example, lymphedema, at a single-cell resolution.

In this study, we performed scRNA-seq of 70,209 cells of the SVF of subcutaneous adipose tissues from patients with cancer-associated lymphedema and healthy donors. We sought to identify the cellular subpopulations associated with the disease, lineage-specific regulatory changes, and intercellular communication alterations in adipose tissues of lymphedema. The ultimate purpose of this study was to find novel medical targets or therapies for the prevention or treatment of lymphedema.

Results

scRNA-seq reveals cellular diversity and heterogeneity of subcutaneous adipose tissues in cancer-associated lymphedema

To unbiasedly dissect cellular heterogeneity of the SVF of adipose tissues under healthy and diseased conditions, we obtained subcutaneous adipose tissue specimens from the affected thighs of 5 patients with severe lymphoedema (stage III; the CASE group) following surgical intervention

for cervical cancer. As a control group (CTRL), liposuction specimens from the thighs of four healthy donors were also collected (Fig. 1a and Supplementary Table S1). There was no significant difference in BMI between the two groups (P value = 0.11, Wilcoxon rank-sum test). After SVF isolation, each fresh sample was subjected to scRNA-seq separately. Following stringent quality filtering, we ultimately obtained transcriptomes of 70,209 cells (CASE: 41,274 cells; CTRL: 28,935 cells). Unbiased clustering revealed 21 clusters (Fig. 1b). Based on hierarchical clustering (Fig. 1c) and established lineage-specific markers (Fig. 1d), we assigned these clusters to 10 cell lineages. The representative molecular signatures of these clusters are shown in Fig. 1e and Supplementary Table S2.

The ASC lineage (marked by *PDGFRA* and *DCN*)¹⁹, including c0, c1, c3, and c5, accounted for a large proportion (49.2%) of the SVF (Fig. 1c), which is comparable with that (55%) reported previously⁶. A large and diverse population of immune cells (49.9%) were found, including both myeloid cells and lymphocytes. The dominant lineage of myeloid cells was macrophages (marked by *ITGAM* and *CD68*)²⁰, which included three subpopulations, i.e., c6, c8, and c11. Another two types of myeloid cells were mast cells (marked by *TPSB2* and *KIT*)²¹ and dendritic cells (DCs). The DCs encompassed clusters of conventional dendritic cells (c19; marked by *LY75*) and plasmacytoid dendritic cells (c18 and c17; marked by *CLEC4C*)²². The lymphocytes included T cells (c2, c4, and c12; marked by *CD3D* and *CD3G*)²³, B cells (c16; marked by *CD79A* and *IGHG2*)²⁴, natural killer (NK) cells (c7 and c10; marked by *KLRB1* and *KLRD1*)²⁵ and natural killer T (NKT) cells (c9 and c15; expressing both NK and T cell markers). Detailed analysis revealed that both c2 and c12 belonged to CD4⁺ helper T cells (marked by *CD4* and *IL7R*; Supplementary Fig. S1). Cluster c12 also exhibited expression of *CTLR4* and *FOXP3* (Supplementary Fig. S1), thus representing a cluster of regulatory T cells (Treg cells)²⁶. Cluster c4 was a cluster of CD8⁺ T cells, reflected by the high expression of *CD8A* and *CD8B* (Supplementary Fig. S1). The NKT cluster c15 expressed high levels of proliferation markers such as *MKI67* and *TOP2A*, thus representing proliferative NKT cells, whereas the NKT cluster c9 belonged to non-proliferative NKT cells (Supplementary Fig. S1). In addition, we identified vascular cells including endothelial cells (c13; marked by *CDH5* and *PECAM1*)²⁷ and pericytes (c20; marked by *RGS5* and *CSPG4*)²⁸. Since not enough lymphatic endothelial cells were identified, they could not be clustered separately.

Differential proportional analysis reveals significantly expanded or contracted cell lineages and subpopulations in SVF associated with cancer-associated lymphedema

Cell lineages that greatly change in relative proportion are probably associated with the pathogenesis of the

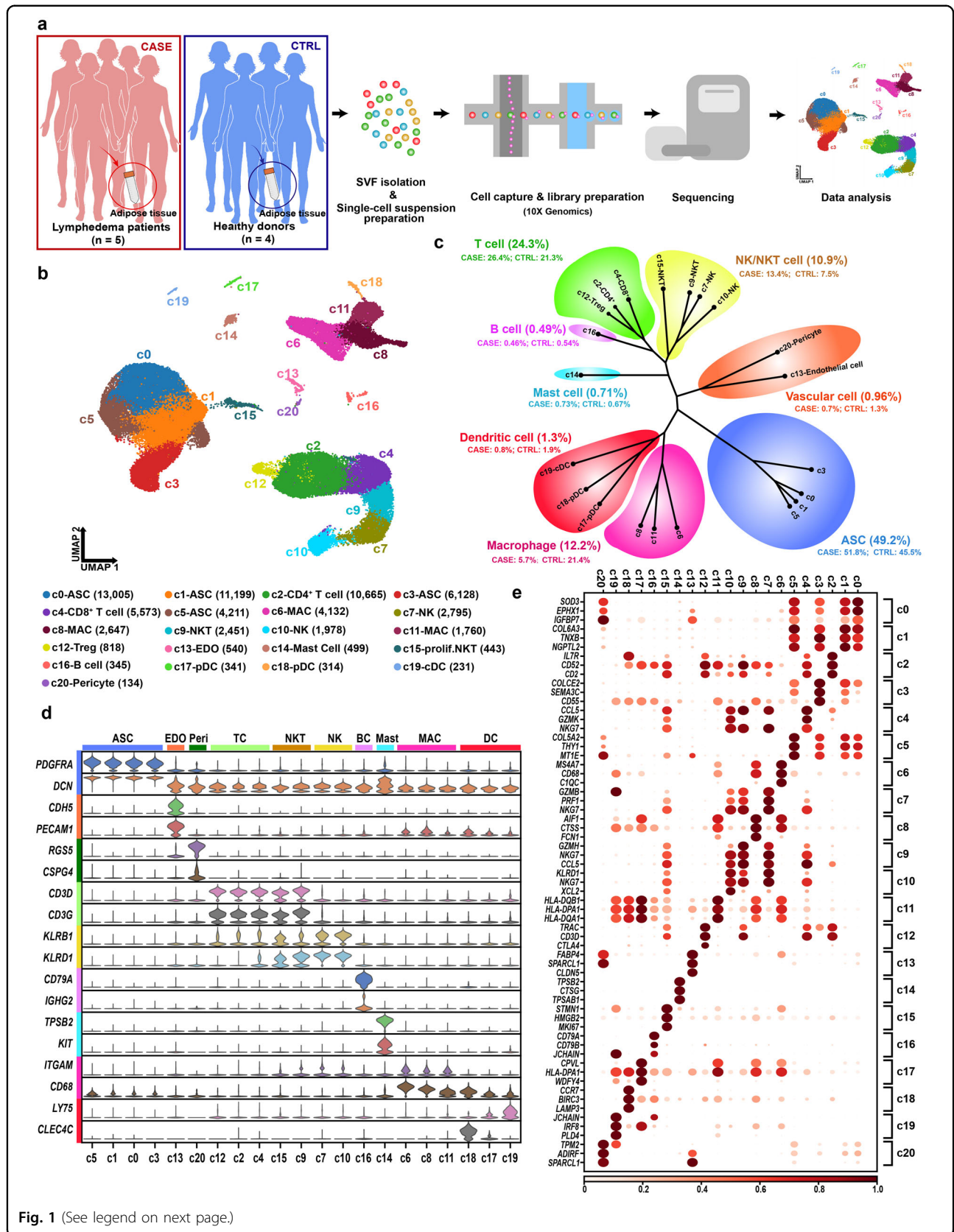


Fig. 1 (See legend on next page.)

(see figure on previous page)

Fig. 1 scRNA-seq reveals cellular diversity and heterogeneity of the SVF of adipose tissues in patients with cancer-related lymphedema.

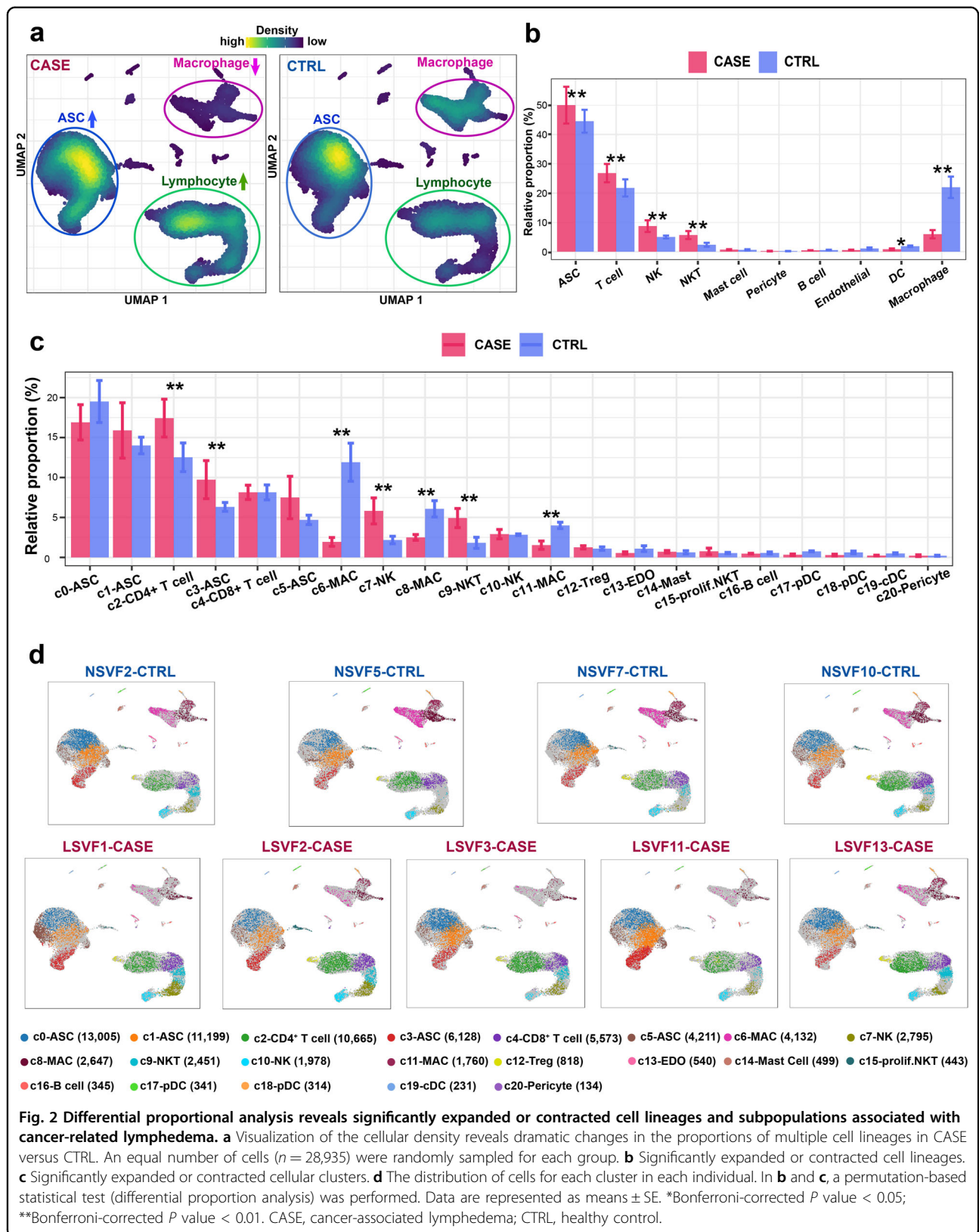
a Schematic representation of the experimental procedure. Patients with cancer-related lymphedema ($n = 5$; the CASE group) and healthy donors ($n = 4$; the CTRL group) were recruited in this study. Liposuction specimens from the thighs were collected during surgery. scRNA-seq was performed separately for each individual. **b** Unbiased clustering of 70,209 cells revealed 21 cellular clusters. The number in parentheses represents the cell count. **c** Hierarchical clustering of the clusters based on the mean expression of the 2000 most variable genes. **d** Expression of the established marker genes for each lineage in each cluster. **e** Representative molecular signatures for each cell cluster. The area of the circles indicates the proportion of cells expressing the gene, and the color intensity reflects the expression intensity. ASC, adipose-derived stromal/stem/progenitor cell; cDC, conventional dendritic cell; EDO, endothelial cell; MAC, macrophage; NK, natural killer cell; NKT, natural killer T cell; prolif.NKT, proliferative nature killer T cell; pDC, plasmacytoid dendritic cell.

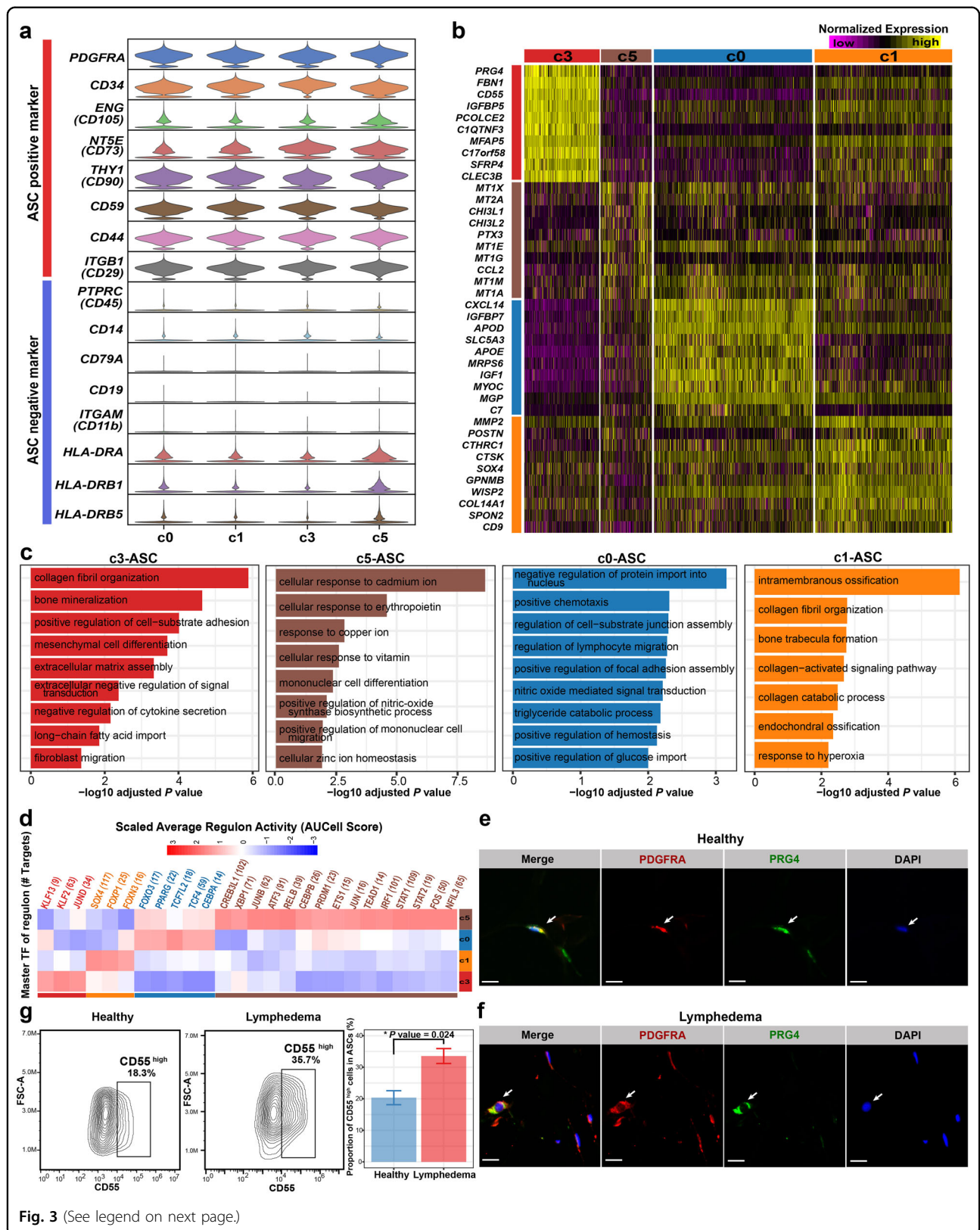
disease. Visualization of the cellular density revealed dramatic changes in the relative proportions of multiple lineages in SVF, including ASCs, macrophages, and lymphocytes (Fig. 2a and Supplementary Fig. S2). To determine whether the change was expected by chance, we performed a permutation-based statistical test (differential proportion analysis) as described previously²⁹. As shown in Fig. 2b, the ASCs were significantly expanded (Bonferroni-corrected P value < 0.01), which suggests enhanced proliferation of ASCs in lymphedema. Indeed, we observed significantly higher cycling scores for ASCs in CASE versus CTRL (P value = $4.916e-09$, Wilcoxon rank-sum test; Supplementary Fig. S3). Strikingly, lymphocyte lineages (T cells, NK, and NKT cells) were significantly expanded, whereas the myeloid lineages (macrophages and DCs) were significantly contracted (Bonferroni-corrected P value < 0.05 , differential proportion analysis; Fig. 2b). This result may reflect enhanced adaptive immunity at the advanced stage of lymphedema. Further analysis at the cluster level revealed significantly expanded subpopulations in SVF, including c2 CD4⁺ T cells; c3 ASCs, c7 NK cells, and c9 NKT cells, reflecting a strong association of these subpopulations with pathogenesis (Fig. 2c, d). The macrophage subpopulation cluster c6 was greatly contracted. Given the results above, we focused on the ASC and macrophage lineages, which may play critical roles in the pathogenesis, in the subsequent analysis.

Heterogeneity of ASCs in the SVF of adipose tissues

We examined the expression of established markers for freshly isolated or cultured ASCs (Fig. 3a). Consistent with our knowledge, *CD34*, a marker for freshly isolated ASCs³⁰, is highly expressed in all ASC subpopulations, suggesting that our isolated cells were close to the in vivo state. The ASCs expressed positive markers for the definition of cultured ASCs (e.g., *CD105*, *CD73*, *CD90*, *CD59*, *CD44*, and *CD29*) and generally lacked expression of negative markers (e.g., *CD45*, *CD14*, *CD11b*, *CD19*, and *CD79A*)^{31,32}. Notably, we found that some ASCs, particularly in cluster c5, expressed MHC class II genes (e.g., *HLA-DRA*, *HLA-DRB1*, and *HLA-DRB5*), suggesting that these cells had antigen-presenting functions. This finding

agrees with the notion that antigen-presenting could be induced under inflammation or disease conditions for ASCs³³. Next, we found that the four subpopulations of ASCs had distinct expression profiles (Fig. 3b and Supplementary Table S3). Cluster c0 expressed high levels of preadipocyte markers such as *CXCL14*, *APOD*, *APOE*, *MGP*, and *WISP2*⁶. The gene signature of c0 was enriched with the term “triglyceride catabolic process” (Fig. 3c). Regulon analysis using SCENIC³⁴ identified *PPARG* and *CEBPA*, the known master TFs in adipogenesis³⁵, as c0-specific regulators (Fig. 3d and Supplementary Table S4). *GGT5*, the maker for committed preadipocytes reported previously³⁶, was highly expressed in c0 (Supplementary Fig. S4). As such, c0 represents committed preadipocytes. Notably, c3, a lymphedema-associated ASC subpopulation that was significantly expanded in SVF (Fig. 2c) and the ASC lineage (Supplementary Fig. S5a), showed high expression of *DPP4* and *CD55*, two markers for multipotent interstitial progenitor cells in adipose tissues³⁶ (Supplementary Fig. S4). It also expressed *PRG4*, which encodes a secreted mucinous glycoprotein³⁷. Its molecular signature was enriched with GO terms such as “collagen fibril organization”, “bone mineralization” and “mesenchymal cell differentiation” (Fig. 3c). As such, c3 may represent interstitial progenitor cells closely associated with the fibrosis of adipose tissues in lymphedema. Through immunofluorescence staining, we confirmed the presence of the *PRG4*⁺ ASCs in subcutaneous adipose tissues of healthy donors (Fig. 3e and Supplementary Fig. S6) and lymphedema patients (Fig. 3f and Supplementary Fig. S6). Based on the spatial distribution in the uniform manifold approximation and projection (UMAP) embedding and the expression of markers (Supplementary Fig. S4), c1 may represent intermediate states between interstitial progenitor and committed preadipocytes. Cluster c5 was an ASC subpopulation displaying a unique pattern with a high expression of metallothionein genes such as *MT1X*, *MT2A*, *MT1E*, *MT1G*, *MT1M*, and *MT1A* (Fig. 3b). Given that metallothionein proteins mainly play roles in protection against damage associated with heavy metal toxicity, endoplasmic reticulum stress, or oxidative stress^{38,39}, c5 may represent a stress-responsive subpopulation. The presence of c1, c3, and c5 cells was also





(see figure on previous page)

Fig. 3 Heterogeneity of ASCs in adipose tissues revealed by single-cell analysis. **a** The expression of marker genes that are normally used for defining freshly isolated or cultured ASCs. **b** Distinct expression profiles of the four subpopulations of ASCs. **c** Enriched Gene Ontology terms of the molecular signature for each subpopulation. Adjusted P value < 0.05 , the hypergeometric test. **d** Subpopulation-specific regulons of each subpopulation obtained by SCENIC analysis. **e** Immunofluorescence staining confirmed the presence of the c3-ASC subpopulation in the subcutaneous adipose tissues of lymphedema patients. Staining was performed in tissue sections of three patients. **f** Immunofluorescence staining confirmed the presence of the c3-ASC subpopulation in the subcutaneous adipose tissues of healthy donors. Staining was performed in tissue sections of two healthy donors. In **e, f**, one representative staining image of one subject is shown. Arrows indicate the $PDGFRA^+PRG4^{high}$ cells. Scale bar: 20 μm . **g** Flow cytometry analyses of the expression of CD55 (a marker for c3-ASC) in ASCs under lymphedema and healthy conditions. A validation cohort (Validation cohort I; $n = 4$ for the lymphedema group and $n = 7$ for the healthy group) independent of the samples subjected to scRNA-seq were used in this analysis. The left two panels show representative contour plots for each group. The bar plot indicates a significantly higher proportion of CD55^{high} cells in ASCs ($PDGFR\alpha^+$) from lymphedema patients than that from healthy donors. Data are presented as means \pm SE. * P value < 0.05 . Wilcoxon rank-sum test. FSC-A forward scatter-area.

confirmed by immunofluorescence staining in the subcutaneous adipose tissue sections from lymphedema patients and healthy donors (Supplementary Figs. S7–S9). In addition, the expression of the markers of the four ASC subpopulations could be observed in cellular subclusters of a published single-cell dataset of human subcutaneous adipose tissue (Supplementary Fig. S10), thus our results represent true heterogeneity in ASCs with improved resolution compared with the previous report (only two subgroups)³⁶. In addition, in a validation cohort (validation cohort I; $n = 4$ for the lymphedema group; $n = 7$ for the healthy group; Age and BMI were matched between groups, P value > 0.05 , Wilcoxon rank-sum test; Supplementary Table S5), through flow cytometry analyses, we confirmed that there was a significantly higher proportion of CD55^{high} cells (c3-ASCs) in ASCs ($PDGFR\alpha^+$) from lymphedema patients than that from healthy donors (Fig. 3g and Supplementary Fig. S11; P value < 0.05 , Wilcoxon rank-sum test).

Dysregulated pathways and genes in the ASCs of cancer-associated lymphedema

scRNA-seq allows unbiased analysis of lineage-specific transcriptomic changes in diseased conditions without cell sorting. We next explored the dysregulated pathways through gene set enrichment analysis (GSEA), which facilitates biological interpretation by robustly detecting concordant differences at the pathway level⁴⁰. Extracellular matrix-related pathways such as “extracellular matrix organization” and “collagen formation” were significantly upregulated (FDR q value < 0.05 , GSEA; Fig. 4a and Supplementary Table S6), which is in line with the fibrosis of adipose tissues in lymphedema. Glycosylation is a common modification of proteins and lipids, which has been implicated in physiological (e.g., cell differentiation) and pathophysiological states (e.g., autoimmunity and chronic inflammation)⁴¹. Strikingly, glycosylation-related pathways such as “O-linked glycosylation” and “diseases of glycosylation” were significantly upregulated, which suggests that increased glycosylation or altered glycosylation patterns in

ASCs may contribute to pathogenesis. In addition, “SUMOylation of DNA damage response and repair proteins” was upregulated, reflecting the DNA damage induced by chronic inflammation⁴². Compared with the healthy condition, ASCs in lymphedema displayed down-regulated protein translation, energy metabolism, and response to endoplasmic reticulum stress (Fig. 4a), reflecting impaired cellular functions at the advanced stage of lymphedema. Unexpectedly, we found decreased adipogenesis for ASCs in lymphedema, as evidenced by the significantly decreased expression of *PPARG* and *CEBPA* (Supplementary Fig. S12a, b), the master regulators in adipogenesis¹⁰ as well as significantly decreased adipogenesis score (P value $< 2.2e-16$, Wilcoxon rank-sum test; Supplementary Fig. S12c). In addition, we found significantly increased osteogenesis of ASCs in lymphedema (Supplementary Fig. S12d), which reflects aberrant differentiation in diseased conditions.

Next, we built gene regulatory networks from the single-cell data using a novel method implemented in bigScale2⁴³ which allows us to quantify the biological importance of genes and find dysregulated genes in diseased conditions. The regulatory networks constructed for ASCs in healthy (upper panel) and diseased conditions (lower panel) are shown in Fig. 4b. Comparative analysis between the two networks revealed a list of genes that were greatly increased in degree centrality (the number of edges connected to a given node; Fig. 4b and Supplementary Table S7) in lymphedema, reflecting their potential roles in the pathogenesis. These genes were mainly involved in bone mineralization, positive regulation of protein kinase B signaling, and regulation of mesenchymal cell proliferation and differentiation (Fig. 4c). Notably, C-Type Lectin Domain Family 3 Member B (*CLEC3B*) ranked at the top of the list based on the changes in degree centrality (Fig. 4d). The expression of *CLEC3B* was upregulated in CASE compared to CTRL (Fig. 4d) and was especially high in the lymphedema-associated subpopulation c3 (Fig. 3b and Supplementary Table S3), which implies that *CLEC3B*

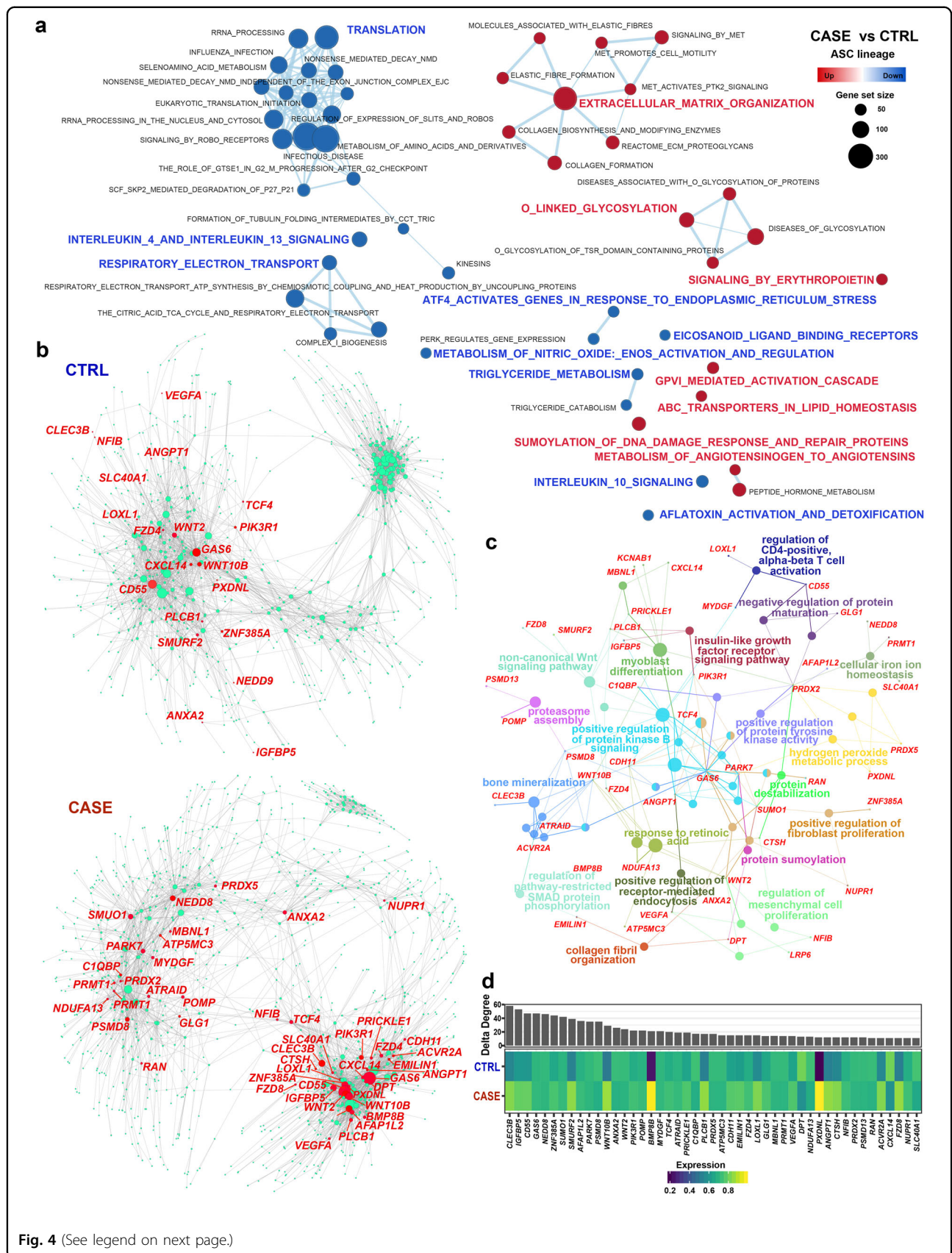


Fig. 4 (See legend on next page.)

(see figure on previous page)

Fig. 4 Dysregulated genes and pathways of ASCs in adipose tissues from cancer-related lymphedema. **a** GSEA reveals upregulated or downregulated pathways of ASCs in CASE versus CTRL. An FDR q value < 0.05 was considered to be statistically significant. **b** Comparative analysis of the gene regulatory networks of ASCs between the CASE (lower panel) and CTRL (upper panel) groups reveals dysregulated genes in ASCs. The node size reflects the degree centrality. The representative genes dysregulated in CASE ranked by delta degree are labeled in red. **c** Network view of the functional enrichment for the dysregulated genes shown in **b**. The small dots denote genes and large nodes represent Gene Ontology terms. The node size represents the number of genes associated with the Gene Ontology term. Adjusted P value < 0.05 . **d** Delta degree centrality (upper panel) and average expression across cells in CASE and CTRL (lower panel). CASE, cancer-associated lymphedema; CTRL, healthy control.

may be associated with fibrosis. The elevated expression of *CLEC3B* was confirmed by using a “pseudobulk” method⁴⁴ (“edgeR-lrt”) implemented in edgeR that accounts for variations among biological replicates (Supplementary Fig. S13a; P value = 0.05). In a validation cohort (validation cohort II, Supplementary Table S5), the expression of *CLEC3B* was significantly upregulated in ASCs freshly isolated from the adipose tissues (passage 0-ASCs) of the lymphedema group ($n = 3$) versus the healthy group ($n = 3$) (Supplementary Fig. S13b; q value = 0.026, differential expression test). In addition, significantly upregulated expression of *CLEC3B* was observed in cultured ASCs (passage 3) from the lymphedema versus normal adipose tissues of patients with secondary lymphedema ($n = 8$) based on the bulk RNA-seq data previously generated by our lab⁴⁵ (Supplementary Fig. S13c; P value = 0.024, Wilcoxon signed-rank test). These evidences support our hypothesis that *CLEC3B* may be a candidate target for lymphedema.

Knockdown of *CLEC3B* could significantly attenuate the fibrogenesis of ASCs from patients

To test the hypothesis that *CLEC3B* is associated with fibrosis, we performed a siRNA-mediated knockdown of *CLEC3B* in ASCs isolated from lymphedema patients (Fig. 5a). The ASCs were in a good state after 96 h of transfection (Fig. 5b). Through bulk RNA-seq, we identified 488 differentially expressed genes between ASCs with the knockdown of *CLEC3B* and the negative control (q value < 0.05 , differential expression test; Supplementary Table S8). The extracellular matrix-related pathways (e.g., “extracellular matrix organization”) were significantly downregulated (adjusted P value < 0.05 , the hypergeometric test; Fig. 5c), suggesting that the fibrogenesis of ASCs was attenuated by the knockdown of *CLEC3B*. Furthermore, we examined the mRNA expression changes of some representative genes determined by bulk RNA-seq (Fig. 5d). Intriguingly, concomitant with the knockdown of *CLEC3B*, the mRNA expression of *PRG4* (one marker of c3 subpopulation) was also significantly downregulated (P value < 0.05 , differential expression test). The expression of the established fibrosis-related genes such as *COL1A1*, *CCN2*, and *FNI* was significantly downregulated. The mRNA expression changes of these genes were confirmed

by quantitative real-time polymerase chain reaction (qPCR; Fig. 5e, P value < 0.05 , paired t -test). In addition, we examined the protein expression changes using immunoblot (Fig. 5f, g). The protein level of *CLEC3B* was significantly decreased by knockdown. The protein levels of Collagen-1 (a fibrosis effector protein), *SMAD2/3*, and phosphorylated *SMAD2/3* (p*SMAD2/3*, the key regulators in the canonical TGF β pathway of fibrosis) were significantly decreased (P value < 0.05 , paired t -test). The mean fluorescence intensity of Collagen-1 staining in ASCs transfected with *CLEC3B* siRNA significantly decreased (Fig. 5h, i, P value < 0.05 , paired t -test). Together, our results suggest that *CLEC3B* could serve as a potential target for alleviating the fibrosis of adipose tissues in lymphedema.

Adipose tissues of lymphedema display a striking depletion of anti-inflammatory macrophages and exhibit a pro-inflammatory microenvironment

We next explored the phenotypic differences among the three lymphedema-associated macrophage subpopulations (c6, c8, and c11). These subpopulations displayed distinct expression profiles (Supplementary Fig. S14a and Table S9). Compared with other subpopulations, c6 showed high expression of *LYVE1*, a marker gene for tissue-resident macrophages⁴⁶. It also displayed a high expression of markers for M2-polarized (alternatively activated) macrophages, including *RNASE1*, *SELENOP*, *MRC1*, and *CD163* (Supplementary Fig. S14b), which harbor an anti-inflammatory phenotype⁴⁷. Thus, the *LYVE1*⁺ c6 cluster represented a resident-like macrophage subpopulation with an M2 phenotype. Compared with the others, cluster c8 expressed higher levels of *IL1B*, a pro-inflammatory cytokine, and markers for M1-polarized (classically activated) macrophages such as *FCGR1A*, *TNF*, and *FPR2*⁴⁸. The *IL1B*^{high} cluster c8 thus represented a pro-inflammatory macrophage subpopulation with an M1 phenotype. Cluster c11 expressed high levels of *CD1C*, encoding an antigen-presenting molecule, and MHC class II genes (e.g., *HLA-DQA1*, *HLA-DPB1*, and *HLA-DPA1*; Supplementary Fig. S14a). It expressed both M1 and M2 markers, e.g., *CD86* and *MRC1*, respectively (Supplementary Fig. S14b). The molecular signature of c11 was enriched with antigen presentation-related terms such as “antigen processing and presentation of exogenous

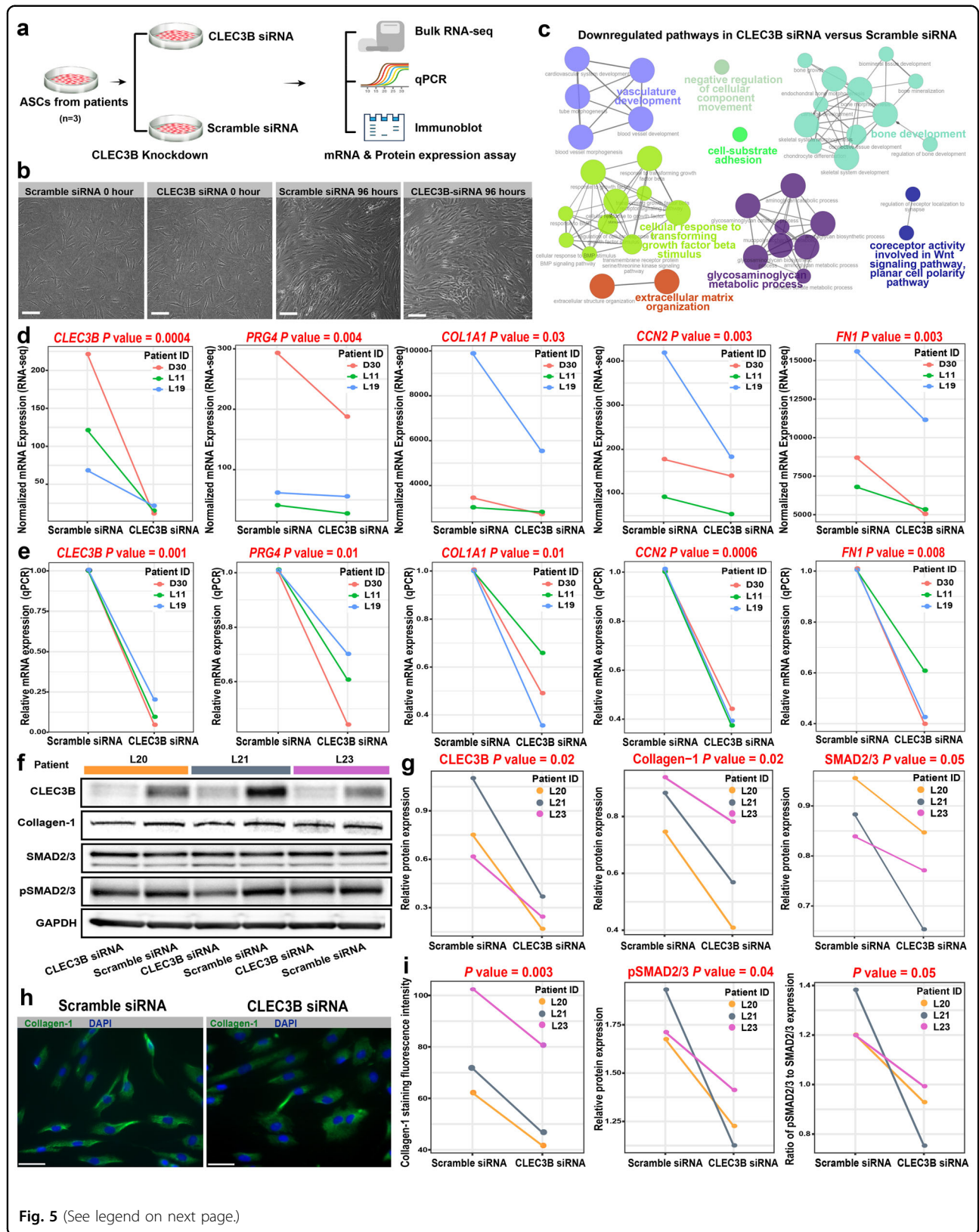


Fig. 5 (See legend on next page.)

(see figure on previous page)

Fig. 5 Knockdown of *CLEC3B* could significantly attenuate the fibrogenesis of ASCs from lymphedema patients. **a** Schematic representation of the experimental procedure. ASCs from patients ($n = 3$) were transfected with *CLEC3B* siRNA or scramble siRNA (negative control). The cells were harvested 48 h and 96 h after transfection for mRNA and protein analysis, respectively. **b** Images showing the ASCs after 96 h of transfection. Scale bar: 100 μm . **c** Network plot showing the downregulated pathways in ASCs with siRNA-mediated knockdown of *CLEC3B* versus the negative control. Functional enrichment analysis was performed on the differential expressed genes detected by bulk RNA-seq. Adjusted P value < 0.05 , the hypergeometric test. **d** Significantly reduced mRNA expression of c3 markers and fibrosis-related genes in ASCs with *CLEC3B* knockdown versus the negative control (determined by bulk RNA-seq). The significance threshold was set to be a P value < 0.05 of the sleuth differential expression test. **e** Significantly reduced mRNA expression of c3 markers and fibrosis-related genes in ASCs with *CLEC3B* knockdown versus the negative control (determined by qPCR). The significance threshold was set to be a P value < 0.05 of the one-tailed paired t -test. **f** Immunoblot assays showing the decreased protein expression of *CLEC3B*, Collagen-1, *SMAD2/3*, and phosphorylated *SMAD2/3* in ASCs with *CLEC3B* knockdown versus the negative control ($n = 3$). **g** Densitometry analysis of the immunoblot results. The significance threshold was set to be a P value < 0.05 of the one-tailed paired t -test. **h** Immunofluorescent staining of Collagen-1 in ASCs transfected with *CLEC3B* siRNA or scramble siRNA. Scale bar: 50 μm . Representative fields of view of ASCs from the patient L21 are shown. **i** Collagen-1 staining fluorescence intensity comparison. Each value represents the mean fluorescence intensity of three representative fields of view. Two-tailed paired t -test.

antigen” (Supplementary Fig. S14c). These results suggest that the *CD1C*^{high} cluster c11 represented a specialized antigen-presenting macrophage subpopulation. Furthermore, we identified subpopulation-specific regulons through SCENIC analysis (Supplementary Fig. S14d and Table S10), for example, *CEBPB*, *FOSL2*, *STAT1*, and *IRF7* for the pro-inflammatory macrophage subpopulation c8. As mentioned above, the macrophage subpopulation c6 was dramatically reduced in SVF (Fig. 2c) and the macrophage lineage under lymphedema (Supplementary Fig. S5b). We calculated the ratio of c6/c8, as a proxy of the ratio of M2/M1, and found that it was greatly decreased in lymphedema (0.76 in CASE versus 2.03 in CTRL), reflecting a pro-inflammatory microenvironment in lymphedema.

Pharmacological blockage of Trem1 using mLR12 could significantly alleviate the lymphedema in a mouse tail model

Given the pro-inflammatory microenvironment of adipose tissues in lymphedema, we next explored the effects of therapies targeting the immune cells. We noted that the pro-inflammatory macrophage subpopulation c8 predominantly expressed *TREM1* (Fig. 6a), which encodes an immune receptor that amplifies the inflammatory response and regulates myeloid recruitment into the inflammatory site⁴⁹. LR12 peptide, a decoy receptor that effectively blocks *TREM1* engagement, has recently been proved to be effective in treating sterile inflammation-related diseases such as atherosclerosis⁵⁰. We thus evaluated the effects of pharmacological blockade of Trem1 using murine LR12 (mLR12) in a widely used mouse tail model of lymphedema. Strikingly, the mouse tail diameter (an indicator of the edema degree) curve of the mLR12 treatment group gradually separated from that of the scramble group following treatment (Fig. 6b). Treated with mLR12, the lymphedema in the mouse tail was greatly alleviated in 6 weeks after the surgery (Fig. 6c). H&E staining of the cross-sections of the mouse tails showed significantly reduced

subcutaneous tissue thickness in the treatment versus the control group (Fig. 6d, e). While collagen fibers were disarrayed in the fibrosis of the scramble group, Sirius red staining showed decreased fibrosis in the treatment group (Fig. 6f). Immunofluorescent staining confirmed the reduced number of Cd11b⁺Trem1⁺ cells in the mouse tail tissue of the treatment group versus the control (Fig. 6g, h). The expression of *Cd68* in the mouse tail tissue of the treatment group was significantly decreased compared with that of the scramble group, indicating reduced infiltration of macrophages and inflammation. In addition, the expression of the genes encoding detrimental cytokines such as *Il1b* and *Tnf* was also significantly decreased with the treatment of mLR12 (Fig. 6j, k). Together, these results suggested that the pharmacological blockage of Trem1 using mLR12 could significantly reduce inflammation and fibrosis, thereby alleviating the lymphedema in mice.

Cell–cell communication analysis uncovers a perivascular ligand-receptor interaction module and communication changes for ASCs in cancer-associated lymphedema

To define the cell–cell communication landscape and uncover its alterations in lymphedema, we performed an analysis using CellPhoneDB 2.0⁵¹. Strikingly, we identified a densely connected communication network among macrophages, ASCs, and vascular endothelial cells in both conditions (Fig. 7a), which is concordant with our knowledge that macrophages, especially *LYVE1*⁺ macrophages⁴⁶, and ASCs⁵² are spatially associated with the blood vasculature. In line with this, we found that ASCs were the predominant source of the macrophage colony-stimulating factor *CSF1* (Supplementary Fig. S15a), which is critical for the survival of macrophages⁵³. The expression of *CSF1* in ASCs was significantly higher in lymphedema than in the healthy condition (Supplementary Fig. S15b), reflecting enhanced signals broadcast by ASCs under the diseased condition. We, therefore, identified a perivascular ligand–receptor signal module. Compared with the healthy condition, the total number of

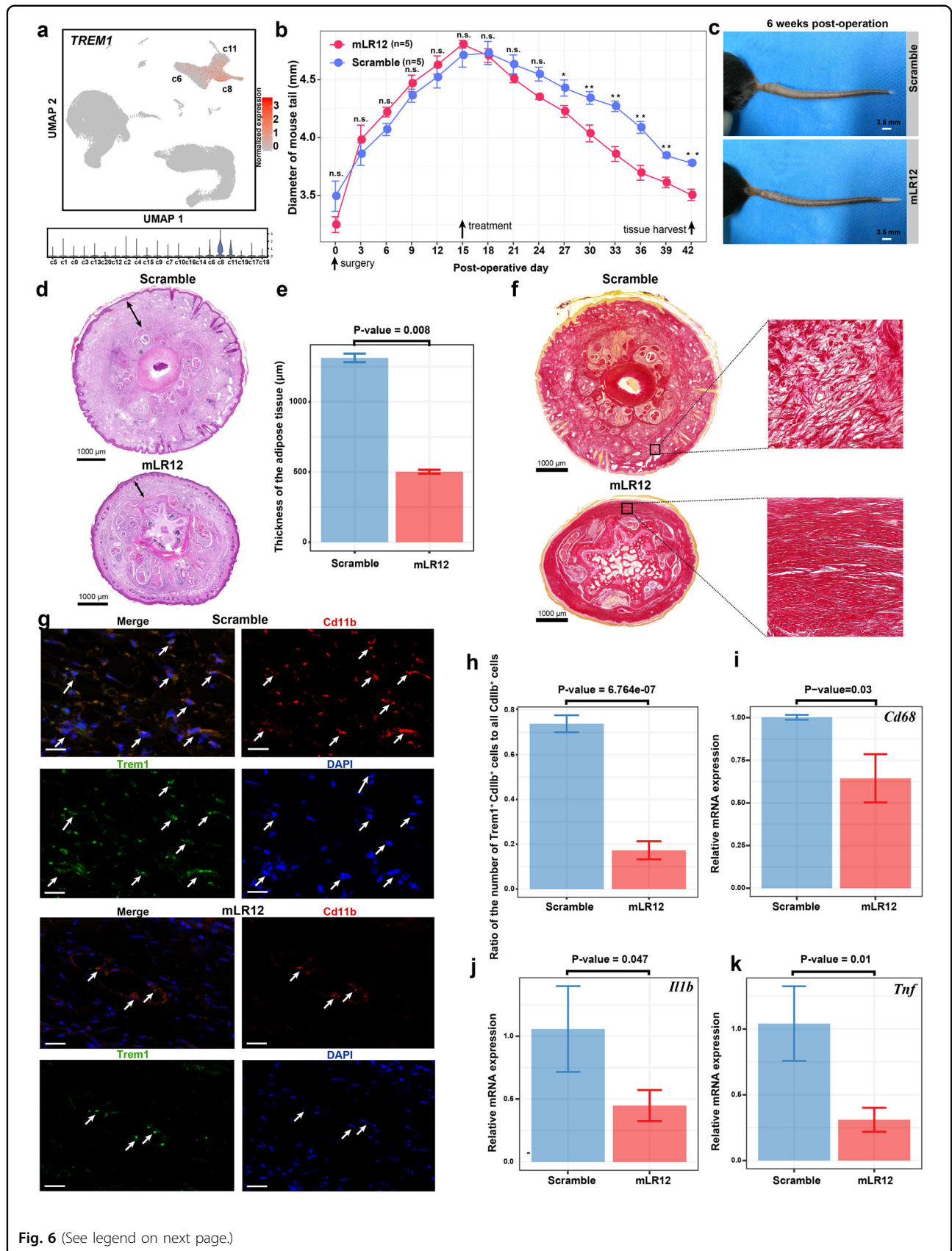


Fig. 6 (See legend on next page.)

(see figure on previous page)

Fig. 6 Pharmacological blockage of Trem1 using mLR12 could significantly alleviate the lymphedema in a mouse tail model. **a** *TREM1* is predominantly expressed by the pro-inflammatory macrophage subpopulation c8. **b** Changes in the diameter of mouse tail during the treatment using mLR12 ($n = 5$) or mLR12-scramble peptides as a control ($n = 5$). Starting from 15 days after the surgery, mice were treated daily by intraperitoneal injection. The diameter of the tail (1 cm distal to the incision) was measured every 3 days for 6 weeks. Tail tissue samples were collected 6 weeks after the surgery for subsequent assays. * P value < 0.05, ** P value < 0.01, n.s. not significant, one-tailed t -test. **c** Images showing the mouse tails following treatment. **d** H&E staining of the cross-sections of the mouse tails showing reduced subcutaneous tissue edema in the treatment versus the control group. The double-sided arrow indicates the thickness of subcutaneous tissues. **e** Thickness of the subcutaneous tissues measured based on the H&E staining images. **f** Sirius red staining showing decreased fibrosis. Collagens were stained in red. Collagen fibers are disarrayed in the fibrosis of the scramble group. **g** Immunofluorescent staining showing a reduced number of Cd11b⁺Trem1⁺ cells in the treatment group (lower panel) versus the control group (upper panel). The arrows indicate the Cd11b⁺Trem1⁺ cells. **h** Proportion of the Cd11b⁺Trem1⁺ macrophages in all Cd11b⁺ cells in the two groups based on the immunofluorescent staining. **i** Reduced mRNA expression of *Cd68* in the mouse tail tissue following the LR12 treatment. **j** Reduced mRNA expression of *Il1b* in the mouse tail tissue following the LR12 treatment. **k** Reduced mRNA expression of *Tnf* in the mouse tail tissue following the LR12 treatment. In **e, h–k**, the significant threshold was set to be a P value of the one-tailed t -test < 0.05 ($n = 3$). In **d, e**, sections at almost the same level (located 1 cm distal to the surgical site) were used for both groups.

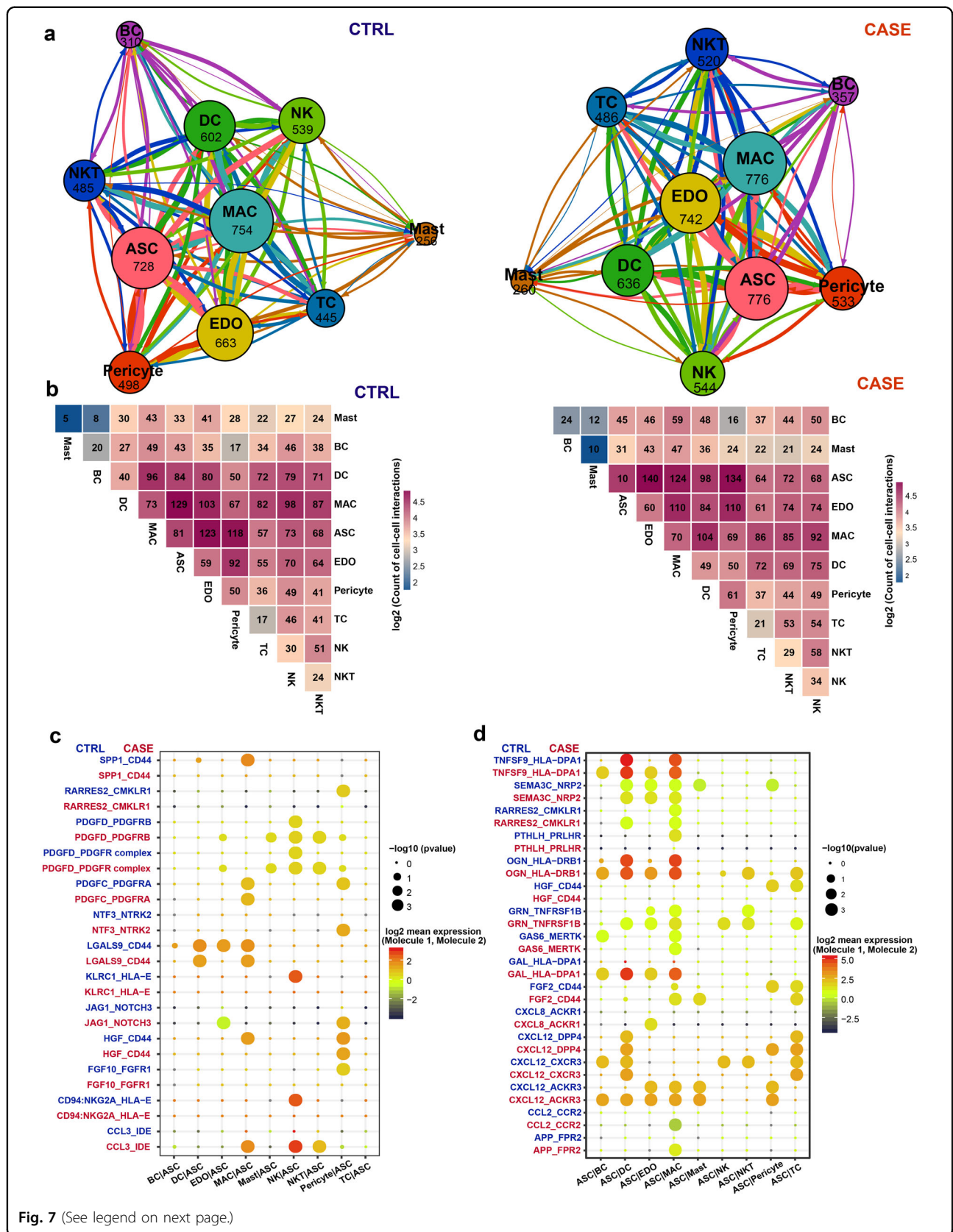
interactions for almost all lineages increased in lymphedema (Fig. 7a), reflecting enhanced intercellular communications in diseased conditions. Notably, the most abundant interactions in the network occurred between ASCs and macrophages under the healthy condition, whereas the most abundant interactions occurred between ASCs and vascular endothelial cells in lymphedema (Fig. 7b). Furthermore, we identified the ligand–receptor pairs showing significant changes in specificity between any one of the non-ASC lineages and ASCs in diseased versus healthy conditions (ASCs express receptors and receive ligand signals from other lineages; Fig. 7c and Supplementary Table S11). Notably, PDGFD–PDGFR complex interactions were significantly enhanced between some lineages (vascular endothelial cells, mast cells, NKT cells, and pericytes) and ASCs in lymphedema. Increased secretion of PDGFD or enhanced PDGFD signaling has been associated with aberrant proliferation and differentiation of fibroblasts in some diseases such as fibrosis and cancer^{54,55}. Our results suggest that PDGFD signaling may contribute to the enhanced fibrosis and proliferation of ASCs in lymphedema. In addition, we also explored the alterations in ligand signals broadcast by ASCs (Fig. 7d). Notably, some chemokine signals broadcast by ASCs, including CXCL8, CXCL12, and CCL2, were significantly altered. For example, CXCL12–ACKR3 interactions between ASCs and BCs or DCs become significantly more specific in lymphedema (permutation test P value < 0.05).

Discussion

Lymphedema is characterized by excess adipose deposition in the affected limbs⁸; however, the underlying mechanism remains elusive. Previous studies suggested enhanced adipogenesis, i.e., the differentiation of adipocytes from ASCs in mouse models¹² and human patients¹⁰, based on a limited number of marker genes. In contrast, our single-cell analysis did not find any significantly upregulated pathways associated with adipogenesis.

Instead, we found that ASCs from lymphedema may have decreased adipogenesis (Supplementary Fig. S12) and enhanced proliferation ability (Supplementary Fig. S3). The enhanced proliferation of ASCs from lymphedema is consistent with the finding of a study based on bulk RNA-seq⁴⁵. Histological evidence has shown that hypertrophic (cell enlargement) adipocytes are frequently observed, especially in the severe stages of lymphoedema⁹. Therefore, we think that the excess adipose deposition may be mostly attributed to the enhanced proliferation ability of ASCs and cell enlargement of adipocytes at least in the severe stage of lymphoedema.

Stage III lymphedema, also known as lymphostatic elephantiasis, is a severe condition in which the tissue becomes extremely swollen, thickened, and fibrotic¹. Concordant with the enhanced fibrosis, we found that the extracellular matrix-related pathways, such as “extracellular matrix organization” and “collagen formation”, were significantly upregulated in ASCs from lymphedema (Fig. 4a). Furthermore, we pinpointed the ASC subpopulation that was closely associated with the pathophysiology of lymphedema, i.e., c3 (*PRG4*^{+/}*CLEC3B*⁺ ASCs), which was significantly expanded in lymphedema. It showed high expression of *DPP4* and *CD55*, two markers for multipotent interstitial progenitor cells in adipose tissue³⁶ (Supplementary Fig. S4b), suggesting that it generally corresponds to multipotent interstitial progenitors. We also noted that the molecular signature of this subpopulation was enriched with pathways such as “collagen fibril organization” and “bone mineralization” (Fig. 3c), suggesting that this subpopulation was related to fibrosis and pathologic mineralization of adipose tissues in lymphedema. However, it does not correspond to fibro-inflammatory progenitors (FIPs) previously identified in visceral white adipose tissue of adult mice⁵⁶, since it expressed high levels of some FIP markers, for example, fibrosis-associated markers, *FNI* and *LOXLI*, but exhibited low expression for other markers, for example, inflammation-associated marker *CCL2* (Supplementary



(see figure on previous page)

Fig. 7 Cell–cell communication analysis reveals a perivascular ligand–receptor interaction module and communication changes for ASCs in cancer-related lymphedema. **a** Intercellular communication networks in the adipose tissues from patients with lymphedema (CASE; right panel) and healthy people (CTRL; left panel). The total number of communications is shown for each cell lineage. The line color indicates that the ligands are broadcast by the cell lineage in the same color. The line thickness is proportional to the number of broadcast ligands. **b** Heatmap shows the number of communications between any two lineages in the CASE (right panel) and CTRL (left panel) groups. **c** The ligand–receptor pairs showing significant changes in specificity between any one of the non-ASC lineages and ASCs in CASE versus CTRL. ASCs express receptors and receive ligand signals from other lineages. The dot size reflects the *p* value of the permutation tests for lineage specificity. The dot color denotes the mean of the average ligand–receptor expression in the interacting lineages. **d** The ligand–receptor pairs showing significant changes in specificity between ASCs and any one of the non-ASC lineages in CASE versus CTRL. ASCs express ligands and broadcast ligand signals for other lineages. ASC, adipose-derived stromal/stem/progenitor cell; BC, B cell; CASE, cancer-associated lymphedema; CTRL, healthy control; DC, dendritic cell; EDO, endothelial cell; MAC, macrophage; NK, natural killer cell; NKT, natural killer T cell; TC, T cell.

Fig. S4c). It has been suggested that the multipotent interstitial progenitors of visceral white adipose tissues were depleted by obesity and/or high-fat feeding³⁶. Our study reported the expansion and dysregulation of the multipotent interstitial progenitors of subcutaneous adipose tissues in response to the pathophysiological stimuli of lymphedema. The balance between multipotent interstitial progenitors and preadipocytes is therefore essential for the homeostasis of adipose tissues. The development of medical therapies to balance the two groups of cells may be a novel therapeutic strategy. We demonstrated that the knockdown of *CLEC3B*, another marker of the c3-ASC subpopulation, could significantly attenuate the fibrogenesis of ASCs from patients in vitro (Fig. 5). Altogether, we identified a potential cellular and molecular target for preventing or treating adipose tissue fibrosis in lymphoedema.

We found a striking depletion of the anti-inflammatory macrophages, i.e., the c6 *LYVE1*⁺ resident-like subpopulation, in the adipose tissues of lymphedema (Figs. 2c and 4b). It has been reported that *LYVE1*⁺ macrophages contributed to the homeostasis of the aorta through the control of collagen deposition by smooth muscle cells, thus preventing arterial stiffness⁴⁶. In addition, our analysis revealed a perivascular ligand–receptor interaction module among ASCs, macrophages, and vascular endothelial cells in adipose tissues (Fig. 7), and found that ASCs were the predominant source of the macrophage colony-stimulating factor CSF1 (Supplementary Fig. S15a). These results reflect the close relationship between macrophages and ASCs in adipose tissues. The depletion of macrophages may contribute to the pathological changes in ASCs in lymphedema. Since the expression of *CSF1* in ASCs was even significantly higher in lymphedema than in healthy controls (Supplementary Fig. S15b), we reason that the mechanism underlying the depletion of macrophages, especially for the *LYVE1*⁺ macrophages, may not be due to pathological changes in ASCs. However, the precise mechanism remains to be explored. It has been reported that targeting immune cell subpopulations, such as CD4⁺ helper T cells⁴, was effective for alleviating lymphedema.

We proposed that transplantation of *LYVE*⁺ anti-inflammatory macrophages could serve as a cellular therapy for cancer-associated lymphedema. Given the experimental difficulties of transplantation of *LYVE*⁺ macrophages, we tried to increase the ratio of M2/M1 macrophages (0.76 in CASE versus 2.03 in CTRL estimated by us) by inhibiting the pro-inflammatory M1 macrophages that highly expressed *TREM1*. We proved that the pharmacological blockage of Trem1 using mLR12 could significantly alleviate the lymphedema in a mouse tail model (Fig. 6). These results highlight the importance of anti-inflammatory therapies in lymphedema.

In summary, we provided a comprehensive analysis of the cellular heterogeneity, lineage-specific regulatory changes, and intercellular communication alterations of the SVF in adipose tissues from cancer-associated lymphedema at a single-cell resolution. Our study revealed lymphedema-associated cell subpopulations and a strong depletion of *LYVE*⁺ anti-inflammatory macrophage in lymphedema. We demonstrated that the knockdown of *CLEC3B* could significantly attenuate the fibrogenesis of ASCs from patients, and thus *CLEC3B* could serve as a potential target for alleviating adipose tissue fibrosis in lymphedema. In vivo experiments in mice suggested that pharmacological blockage of *TREM1* using LR12 could serve as a promising medical therapy for treating lymphedema.

Materials and methods

Ethics approval

All human subject recruitments, tissue sampling procedures, and animal experiments have been approved by the ethics committee of Peking Union Medical College Hospital (JS-2528). Each subject provided written informed consent. All applicable institutional and/or national guidelines for the care and use of animals were followed.

Adipose tissue specimen preparation and liposuction

Adipose tissue specimens were obtained from the affected thighs of five female patients with secondary lymphoedema (stage III) following surgical intervention

for cervical cancer. As a control group, liposuction specimens from the thighs of four healthy female donors were collected during surgery for cosmetic purposes. The liposuction procedures used for both groups were the same and the surgeries of both groups were performed in the same division of plastic surgery. General anesthesia was done before liposuction. In total, 1000 ml tumescent solution containing 0.025% lidocaine and 1:1,000,000 epinephrine was injected into the thigh. Satisfactory infiltration of the tumescent solution was indicated by issue blanching and moderate tension. Liposuction was performed with 3-mm blunt-tip cannulas and 20 ml syringes in the deep fat layer. The syringes were stood up for 10 min to separate adipose from a tumescent fluid. Harvested adipose tissues were transferred into 50-ml sterile centrifuge tubes containing 20 ml Dulbecco's Modified Eagle's Medium (10569044, Gibco) cell culture medium, and transported on ice.

SVF isolation and cell viability assay

Each fresh specimen was subjected to SVF isolation. Briefly, each specimen was washed several times with Hank's balanced salt solution (14025126, Gibco). Subsequently, it was digested with 0.15% collagenase I (17100017, Gibco) supplied with 4% Penicillin-Streptomycin (15140122, Gibco) at 37 °C for 30 min. The pellet was resuspended in high-glucose Dulbecco's Modified Eagle's Medium (10569044, Gibco) with 10% fetal bovine serum (10099141, Gibco), filtered through a 100- μ m strainer, and then centrifuged at 4 °C for 5 min. The obtained cell suspensions were resuspended in Hank's balanced salt solution, and red blood cell lysis buffer was added at room temperature for 5 min to remove red blood cells. Then, it was centrifuged again, resuspended in Hank's balanced salt solution with 0.04% bovine serum albumin (A1933-5G, Sigma), and filtered through a 40- μ m strainer. Finally, the cells were centrifuged and resuspended in Dulbecco's Phosphate Buffered Saline without Ca^{2+} and Mg^{2+} (14190144, Gibco). The obtained single-cell suspension was incubated with an equal volume of AOPI Staining Solution (Logos Biosystems). Cell concentration and viability were assayed using a LUNA-FL Fluorescence Cell Counter (Logos Biosystems). The cell viability of all samples subjected to scRNA-seq reached more than 90%.

Animal model and treatment

To model lymphedema, we applied a widely used mouse tail model as previously described⁴. Briefly, the superficial and deep lymphatic channels of the tails of adult male (4–6-week-old, C57) mice were disrupted by a skin incision. Following the surgery, the mice were allowed to recover for 2 weeks and then randomized to scramble ($n = 5$) or treatment ($n = 5$) groups. To pharmacologically inhibit Trem1, a dodecapeptide, murine LR12 (LQEEDTGEYGCV; mLR12)⁵⁷

was chemically synthesized (SBS Genetech, China) and COOH terminally amidated. The endotoxin was below 0.5 EU/mg. Starting from 2 weeks after the incision, mice were treated daily by intraperitoneal injection of mLR12 (5 mg/kg) for 6 weeks. As a control, mice were intraperitoneally injected daily with mLR12-scramble peptides. The diameter of the tail (1 cm distal to the incision) was measured every 3 days for 6 weeks. Tail tissue samples were collected 6 weeks after the surgery for subsequent assays.

scRNA-seq

Freshly isolated SVF cells of each sample were subjected to scRNA-seq capture separately. Chromium Single-Cell 3' Reagent Kit v3 chemistry (10 \times Genomics, USA) was used for single-cell Gel Beads-in-Emulsion (GEM) generation, post-GEM-RT cleanup, barcoding, cDNA amplification, and cDNA library construction according to the manufacturer's protocol. The NovaSeq 6000 system (Illumina, USA) was utilized to sequence the libraries.

scRNA-seq data preprocessing

Sample demultiplexing, barcode processing, and unique molecular identifier (UMI) counting were performed using the official software Cell Ranger v3.0.2. Briefly, the pipeline "cellranger mkfastq" was used to demultiplex the raw base call files generated by the sequencers into reads in FASTQ format. Subsequently, a gene-barcode matrix for each library was generated using the pipeline "cellranger count" pipeline. Lastly, the pipeline "cellranger aggr" was used to concatenate the gene-cell UMI count matrices of all samples into one matrix. The concatenated gene-cell barcode matrix was imported into Seurat v3.1.0 for data preprocessing. Genes with counts in fewer than 3 cells were filtered out to exclude genes detected from random noise. Cell outliers ($<$ first quartile $- 1.5 \times$ interquartile range or $>$ third quartile $+ 1.5 \times$ interquartile range) were filtered out according to expressed genes number, UMI count sum, and the proportion of mitochondrial genes to exclude poor-quality cells. We also filtered out doublets using the predictions by Scrublet⁵⁸. We also excluded the cells enriched in hemoglobin gene expression. We normalized the sum of the UMI counts for each cell to 10,000 and then log-transformed the data. For each sample, the "FindVariableFeatures" function of Seurat was used to select 2000 features (genes). All the datasets were integrated via canonical correlation analysis implemented in Seurat to correct for potential batch effects. The mitochondrial gene proportion, S phase score, G2M phase score, and UMI count were regressed out with linear models to mitigate the effects of uninteresting sources of variation.

Dimensional reduction and clustering of the scRNA-seq data

Linear dimensional reduction of the scRNA-seq data was performed through principal component analysis

(PCA). A neighborhood graph of the cells was computed using the first 30 PCA components. Using UMAP⁵⁹, the neighborhood graph was embedded in a two-dimensional space. The cells were clustered using Louvain clustering (resolution = 0.6) implemented in Seurat.

Differential expression and functional enrichment analysis

The likelihood-ratio test (test.use: “bimod”) implemented in the function “FindMarkers” of Seurat was utilized to detect differentially expressed genes of the scRNA-seq data between two groups. The significance threshold was set to a log₂-fold change > 0.25 and an adjusted *P* value < 0.05. The differential expression of candidate targets was confirmed by using a “pseudobulk” method⁴⁴ (“edgeR-lrt”) implemented in the R package edgeR under default settings, which aggregates read counts across the single cells of the scRNA-seq data and accounts for variations among biological replicates. Functional enrichment analyses of a gene list were carried out using ClueGO⁶⁰ with an adjusted *P* value < 0.05.

Gene set enrichment analysis

Signal2Noise (the difference in means between CASE and CTRL scaled by the standard deviation) was applied to pre-rank all the expressed genes. The ranked gene list was then imported into the software GSEA (version: 4.0.1)⁶¹. The statistical significance cutoff was set to an FDR *q* value < 0.05. The precompiled REACTOME pathways in MSigDB (version: 7.0)⁶² were applied. We visualized the analysis results using the EnrichmentMap plugin of Cytoscape (version: 3.7.0).

Differential proportion analysis

A permutation-based statistical test (differential proportion analysis) was performed as described previously²⁹ to determine whether the change in relative proportions was expected by chance. The statistical significance threshold was set to a *P* value with Bonferroni correction < 0.05.

Differential regulatory network analysis

Using the method implemented in bigScale2⁴³, the single-cell transcriptomic data was used to build gene regulatory networks and comparative analysis was performed between the two groups. Briefly, the “compute.network” function (clustering = “direct”, quantile.p = 0.90) was used to infer gene regulatory networks separately for the CASE and CTRL. Genes encoding mitochondrial proteins or ribosomal proteins were excluded. Subsequently, using the function “homogenize.networks”, the number of edges was homogenized throughout the inferred networks. Lastly, using the function “compare.centralities”, we identified the changes in node centralities (the relative importance of genes in the network) in the CASE. Four measures of

centrality were considered, including betweenness, degree, pagerank, and closeness.

Subpopulation-specific regulon analysis

We performed regulon analysis using the R package SCENIC³⁴ to identify the master regulators driving the cellular heterogeneity among subpopulations. Briefly, coexpression modules that included a set of genes coexpressed with regulators were identified. Only the modules with significant motif enrichment of the regulators (referred to as regulons) were retained. Each cell was scored for the activity of each regulon. According to the average regulon activity scores of cells in the subpopulation, subpopulation-specific regulons were identified.

Cell–cell communication analysis

CellPhoneDB 2.0⁵¹, which allows for statistically inferring lineage-specific interactions, was applied to analyze cell–cell communication according to the single-cell transcriptomic dataset. Briefly, ligand–receptor interactions were predicted according to the expression of a receptor by one lineage and a ligand by another. We only considered the ligands and receptors expressed in greater than 10% of the cells in any given cell type. To generate a null distribution for each ligand–receptor pair in each pairwise comparison between lineages, we randomly permuted the labels of all cells 1000 times and calculated the means of the average ligand–receptor expression in the interacting cell types. A *P* value for the likelihood of lineage specificity was ultimately obtained for each ligand–receptor pair.

Knockdown of *CLEC3B* expression in ASCs

ASCs were cultured in complete medium, i.e., Dulbecco’s modified Eagle’s medium (11885084, Gibco) supplemented with 10% fetal bovine serum (10099141, Gibco) and 1% Penicillin-Streptomycin (15140122, Gibco), at 37 °C with 5% CO₂. Before the transfection, the cells were trypsinized and counted. Then, the cells were diluted in an antibiotic-free culture medium, plated into 6-well plates, and incubated at 37 °C with 5% CO₂ overnight. ON-TARGETplus Human *CLEC3B* siRNA Smartpool (L-019749-00-0005, Horizon) was synthesized to knockdown the expression of *CLEC3B*. ON-TARGETplus non-targeting pool was used as a negative control (Scramble siRNA, D-001810-10-05, Horizon). The ON-TARGETplus siRNA technology reduces off-targets through strand modifications and seed-region analysis on siRNA design. Cell transfection was carried out using the DharmaFECT 4 siRNA Transfection Reagent (T-2004-02, Dharmacon) according to the manufacturer’s instructions. The cells were plated in an antibiotic-free culture medium with 25 nM siRNA concentrations at 37 °C with 5% CO₂. The culture medium was changed into an antibiotic-containing

medium 24 h after transfection. The cells were collected at 48 h for mRNA analysis and 96 h for protein analysis.

Bulk RNA-seq and data analysis

After the incubation for 48 h, the cells were harvested for total RNA extraction using TRIzol reagent (15596018, Invitrogen). A NEBNext Ultra RNA Library Prep Kit for Illumina (E7530L, NEB) was used for bulk RNA-seq library construction. The libraries were subjected to sequencing using the Illumina X Ten system. Following quality control with fastp⁶³, the sequencing reads were subjected to transcript abundance quantification with kallisto⁶⁴. Differentially expressed genes between groups were identified using sleuth⁶⁵. The statistical significance cutoff was set to a *q* value of 0.05.

RNA extraction and gene expression assay with qPCR

The total RNA from the cells or the mouse tail tissues was extracted with TRIzol reagent (15596018, Invitrogen). Single-stranded DNA was synthesized using PrimeScript Reverse Transcriptase (2680A, TaKaRa). qPCR was performed using the PowerUpTM SYBRTM Green Master Mix (A25742, Applied Biosystems). *GAPDH* was used as a reference gene. The relative levels of mRNAs were calculated by the $2^{-\Delta\Delta Ct}$ method. All primers used are listed below: *CLEC3B*, 5'-GCCTCTTCTCCCTCCTGAC-3' (forward) and 5'-ATCTTTGTGTTCAACAACATCTTTCT-3' (reverse); *PRG4*, 5'-AGTTTCATCTCAAGAGCTTTCCTGT-3' (forward) and 5'-GGTGATGTGGGATTATGCAC TTCTG-3' (reverse); *FNI*, 5'-GAGAATAAGCTGTACCATCGAA-3' (forward) and 5'-CGACCACATAGGAAGTCCAG-3' (reverse); *CCN2*, 5'-CAGCATGGACGTTCGTCTG-3' (forward) and 5'-AACCACGGTTTGGTCCTTG G-3' (reverse); *COL1A1*, 5'-GAGGGCCAAGACGAAGACATC-3' (forward) and 5'-CAGATCACGTCATCGCACAAC-3' (reverse); *GAPDH*, 5'-CTATAAATTGAGCCC GCAGCC-3' (forward) and 5'-GCCCAATACGACCAAA TCCGT-3' (reverse); *Cd68*, 5'-TGCTGATCTTGCTAGGACCG-3' (forward) and 5'-GAGAGTAACGGCCTTTTT GTGA-3' (reverse); *Tnf*, 5'-TAGCCACGTCGTAGCAAAC-3' (forward) and 5'-GCAGCCTTGTCCTTGAAGA-3' (reverse); *Il1b*, 5'-TGCCACCTTTTGACAGTGATGA-3' (forward) and 5'-GCTCTTGTTGATGTGCTGCTG-3' (reverse); *Gapdh*, 5'-TCGTCCCGTAGACAAAATGG-3' (forward) and 5'-TTGAGGTCAATGAGGGGGTCC-3' (reverse).

Immunoblot assay

Cultured ASCs were lysed on ice in NP-40 Lysis Buffer (P0013F, Beyotime) containing protease and phosphatase inhibitor. Lysate protein concentrations were determined with Micro BCA Protein Assay Kit (23235, Thermo Scientific). In total, 200–400 μ g of protein per sample (*n* = 3) was used for western blotting analysis. Proteins were

separated by 4%–12% Bis-Tris Bolt gels (NW04120BOX, Invitrogen) and transferred to pure nitrocellulose blotting membranes (66485, Pall Life Sciences). Membranes were blocked with 5% nonfat milk (P0216, Beyotime) or 3% bovine serum albumin (ST023, Beyotime) in Tris-Buffered Saline with Tween-20 (ST671, Beyotime) at room temperature for 1 h. Target proteins were incubated overnight at 4 °C with the following primary antibodies: CLEC3B (ab51883, Abcam), Type I Collagen (ab138492, Abcam), SMAD-2/3 (3102S, Cell Signaling Technology), and phosphorylated SMAD-2/3 (8828S, Cell Signaling Technology). HRP-conjugated corresponding secondary antibodies (ZB-2301/2305, ZSGB-BIO) were used at room temperature for 1 h, followed by chemiluminescent detection (P0018AM, Beyotime). Equal loading controls were indicated with GAPDH (2118L, Cell Signaling Technology). Densitometry analysis was performed by quantifying the intensity of the bands using the ImageJ software.

Paraffin section preparation

Adipose tissues from patients or mouse tail tissues were isolated and fixed in 4% paraformaldehyde (DF0135, LEAGENE). The mouse tail tissues were decalcified in 10% neutral buffered EDTA (DD0002, LEAGENE) at 37 °C for 2 weeks. The adipose tissues and mouse tail tissues were dehydrated by ASP300S (Leica) and then were paraffin-embedded. The wax blocks were cut into 5- μ m sections with RM2235 (Leica) for the subsequent staining. For all the staining experiments of mouse tail tissues, cross-sections of the mouse tails at almost the same level (located 1 cm distal to the surgical site) were used for both groups. The staining results were visualized on the Panoramic SCAN (3DHISTECH) or the Vectra Polaris pathology imaging system (PerkinElmer).

H&E staining

H&E staining was conducted using routine protocols on the Varistain Gemini automatic stainer (Thermo Fisher Scientific). Subcutaneous tissue thickness analysis was performed to measure the distance from the basal layer of the epidermis to the deep fascia. A total of three representative regions per section were analyzed using the ImageJ software.

Sirius red staining

The sections were incubated with hematoxylin solution for 5 min, 0.1% Sirius red solution for 1 h, dehydrated in absolute alcohol, cleared in xylene, and mounted with neutral balsam. Collagen and non-collagen components were stained in red and yellow, respectively.

Immunofluorescent staining of tissue sections and cultured cells

Tissue sections were deparaffinized, and then the antigen was repaired with EDTA solution (pH = 9.0) or

sodium citrate (pH = 6.0) under high pressure for 2 min. Subsequently, the sections were blocked with 10% goat serum at room temperature for 1 h, followed by primary antibodies at 4 °C overnight. Sections were washed three times with Phosphate Buffered Saline, and then stained with Alexa Fluor 488 goat anti-rabbit (A-11008, Invitrogen) and Alexa Fluor 594 goat anti-mouse (ab150116, Abcam) secondary antibodies at room temperature for 40 min. The sections were sealed with 4',6-diamidino-2-phenylindole (DAPI) mounting solution (ZLI-9557, ZSGB-BIO). The primary antibodies used for immunofluorescent staining included: PRG4 (ab28484, Abcam), CHI3L1 (ab77528, Abcam), CTHRC1 (ab85739, Abcam), CXCL14 (ab46010, Abcam), PDGFR α (MAB322, R&D), Cd11b (ab8878, Abcam), and Trem1 (bs-4886R, Bioss).

Cultured cells were fixed in 4% paraformaldehyde (DF0135, LEAGENE) for 10 min at room temperature, and permeabilized with 0.2% Triton X-100 (A110694-0100, Diamond) in Phosphate Buffered Saline for 20 min. Thereafter, cells were blocked with 3% bovine serum albumin (A1933-5G, Sigma) in Phosphate Buffered Saline for 1 h, followed by primary antibody Collagen-1 (ab138492, Abcam) at 4 °C overnight. Cells were then stained with Alexa Fluor 488 goat anti-rabbit (A-11008, Invitrogen) secondary antibody at room temperature for 1 h. DAPI (4083S, Cell Signaling Technology) was used for nuclear counterstaining. The cells were imaged using the Axio Vert.A1 Microscope (ZEISS). Mean fluorescence intensity was measured using the ImageJ software.

Flow cytometry

SVF was resuspended in cell staining buffer (420201, BioLegend), and then incubated with the following cellular surface antibodies at room temperature in the dark for 30 min: PDGFR α (CD140a)-Phycoerythrin (323506, BioLegend) and CD55-Allophycocyanin (311312, BioLegend). The cells were washed twice with cell staining buffer to remove unbound antibodies. Flow cytometry data were acquired on the Accuri C6 flow cytometer (BD Biosciences) and analyzed using the FlowJo software (BD Biosciences).

Acknowledgements

We thank AegleStem Therapeutics Co., Ltd. for organizing the animal experiments. This work was supported by grants from the National Natural Science Foundation of China (81870229, 81900282) and CAMS Innovation Fund for Medical Sciences (2021-I2M-1-008).

Author details

¹State Key Laboratory of Cardiovascular Disease, Beijing Key Laboratory for Molecular Diagnostics of Cardiovascular Diseases, Center of Laboratory Medicine, Fuwai Hospital, National Center for Cardiovascular Diseases, Chinese Academy of Medical Sciences and Peking Union Medical College, Beijing, China. ²Prenatal Diagnosis Center, Department of Obstetrics and Gynecologic, Key Laboratory of Birth Defects and Related Diseases of Women and Children, Ministry of Education, West China Second University Hospital, Sichuan University, Chengdu, Sicuan, China. ³Division of Plastic Surgery, Peking Union Medical College Hospital, Beijing, China

Author contributions

Conceptualization: X. Liu and F.X.; Data curation: X. Liu; Formal analysis: X. Liu; Funding acquisition: Z.Z. and X. Liu; Investigation: X. Liu and M.Y.; Methodology: X. Liu, M.Y., Q.X. and W.C.; Project administration: Z.Z. and X. Long; Resources: Z.L., J.H., J.C. and N.Y.; Software: X. Liu; Supervision: Z.Z. and X. Long; Validation: M.Y.; Visualization: X. Liu; Writing, original draft preparation: X. Liu and M.Y.; Writing, review and editing: X. Liu and M.Y.

Data availability

Datasets related to this article can be found at <https://ngdc.cnbc.ac.cn/gsa-human/browse/HRA000901>, hosted at Genome Sequence Archive.

Conflict of interest

The authors declare no competing interests.

Publisher's note

Springer Nature remains neutral with regard to jurisdictional claims in published maps and institutional affiliations.

Supplementary information The online version contains supplementary material available at <https://doi.org/10.1038/s41421-022-00402-5>.

Received: 8 October 2021 Accepted: 9 March 2022

Published online: 21 June 2022

References

- Lawenda, B. D., Mondry, T. E. & Johnstone, P. A. S. Lymphedema: a primer on the identification and management of a chronic condition in oncologic treatment. *CA Cancer J. Clin.* **59**, 8–24 (2009).
- Rockson, S. G., Keeley, V., Kilbreath, S., Szuba, A. & Towers, A. Cancer-associated secondary lymphoedema. *Nat. Rev. Dis. Prim.* **5**, 22 (2019).
- DiSipio, T., Rye, S., Newman, B. & Hayes, S. Incidence of unilateral arm lymphoedema after breast cancer: a systematic review and meta-analysis. *Lancet Oncol.* **14**, 500–515 (2013).
- Zampell, J. C. et al. CD4+ cells regulate fibrosis and lymphangiogenesis in response to lymphatic fluid stasis. *PLoS ONE* **7**, e49940 (2012).
- Shaitelman, S. F. et al. Recent progress in the treatment and prevention of cancer-related lymphedema. *CA Cancer J. Clin.* **65**, 55–81 (2015).
- Vijay, J. et al. Single-cell analysis of human adipose tissue identifies depot- and disease-specific cell types. *Nat. Metab.* **2**, 97–109 (2020).
- Ramakrishnan, V. M. & Boyd, N. L. The adipose stromal vascular fraction as a complex cellular source for tissue engineering applications. *Tissue Eng. Part B Rev.* **24**, 289–299 (2018).
- Mehrra, B. J. & Greene, A. K. Lymphedema and obesity: Is there a link? *Plast. Reconstr. Surg.* **134**, 154e–160e (2014).
- Tashiro, K. et al. Pathological changes of adipose tissue in secondary lymphoedema. *Br. J. Dermatol.* **177**, 158–167 (2017).
- Januszyk, M. et al. Molecular analysis and differentiation capacity of adipose-derived stem cells from lymphedema tissue. *Plast. Reconstr. Surg.* **132**, 580–589 (2013).
- Zampell, J. C. et al. Regulation of adipogenesis by lymphatic fluid stasis: Part I. Adipogenesis, fibrosis, and inflammation. *Plast. Reconstr. Surg.* **129**, 825–834 (2012).
- Aschen, S. et al. Regulation of adipogenesis by lymphatic fluid stasis: Part II. Expression of adipose differentiation genes. *Plast. Reconstr. Surg.* **129**, 838–847 (2012).
- Zheng, G. X. Y. et al. Massively parallel digital transcriptional profiling of single cells. *Nat. Commun.* **8**, 14049 (2017).
- Kulkarni, A., Anderson, A. G., Merullo, D. P. & Konopka, G. Beyond bulk: a review of single cell transcriptomics methodologies and applications. *Curr. Opin. Biotechnol.* **58**, 129–136 (2019).
- Reyfman, P. A. et al. Single-cell transcriptomic analysis of human lung provides insights into the pathobiology of pulmonary fibrosis. *Am. J. Respir. Crit. Care Med.* **199**, 1517–1536 (2019).
- Der, E. et al. Tubular cell and keratinocyte single-cell transcriptomics applied to lupus nephritis reveal type I IFN and fibrosis relevant pathways. *Nat. Immunol.* **20**, 915–927 (2019).

17. Burl, R. B. et al. Deconstructing adipogenesis induced by beta3-Adrenergic receptor activation with single-cell expression profiling. *Cell Metab.* **28**, 300–309.e4 (2018).
18. Schwäbe, P. C. et al. A stromal cell population that inhibits adipogenesis in mammalian fat depots. *Nature* **559**, 103–108 (2018).
19. Guerrero-Juarez, C. F. et al. Single-cell analysis reveals fibroblast heterogeneity and myeloid-derived adipocyte progenitors in murine skin wounds. *Nat. Commun.* **10**, 650 (2019).
20. Singhal, S. et al. Human tumor-associated monocytes/macrophages and their regulation of T cell responses in early-stage lung cancer. *Sci. Transl. Med.* **11**, eaat1500 (2019).
21. Vieira Braga, F. A. et al. A cellular census of human lungs identifies novel cell states in health and in asthma. *Nat. Med.* **25**, 1153–1163 (2019).
22. Merad, M., Sathe, P., Helft, J., Miller, J. & Mortha, A. The dendritic cell lineage: ontogeny and function of dendritic cells and their subsets in the steady state and the inflamed setting. *Annu. Rev. Immunol.* **31**, 563–604 (2013).
23. Guo, X. et al. Global characterization of T cells in non-small-cell lung cancer by single-cell sequencing. *Nat. Med.* **24**, 978–985 (2018).
24. Hu, Y., Wang, D., Zhai, K. & Tong, Z. Transcriptomic analysis reveals significant B lymphocyte suppression in corticosteroid-treated hosts with pneumocystis pneumonia. *Am. J. Respir. Cell Mol. Biol.* **56**, 322–331 (2017).
25. Xu, Y. et al. Decrease in Natural Killer cell associated gene expression as a major characteristic of the immune status in the bloodstream of colorectal cancer patients. *Cancer Biol. Ther.* **11**, 188–195 (2011).
26. Li, Z., Li, D., Tsun, A. & Li, B. FOXP3+ regulatory T cells and their functional regulation. *Cell Mol. Immunol.* **12**, 558–565 (2015).
27. Kalucka, J. et al. Single-cell transcriptome atlas of murine endothelial cells. *Cell* **180**, 764–779.e20 (2020).
28. Holm, A., Heumann, T. & Augustin, H. G. Microvascular mural cell organotypic heterogeneity and functional plasticity. *Trends Cell Biol.* **28**, 302–316 (2018).
29. Farbehi, N. et al. Single-cell expression profiling reveals dynamic flux of cardiac stromal, vascular and immune cells in health and injury. *Elife* **8**, e43882 (2019).
30. Suga, H. et al. Functional implications of CD34 expression in human adipose-derived stem/progenitor cells. *Stem Cells Dev.* **18**, 1201–1209 (2009).
31. Gimble, J. M., Katz, A. J. & Bunnell, B. A. Adipose-derived stem cells for regenerative medicine. *Circ. Res.* **100**, 1249–1260 (2007).
32. Dominici, M. et al. Minimal criteria for defining multipotent mesenchymal stromal cells. The International Society for Cellular Therapy position statement. *Cytotherapy* **8**, 315–317 (2006).
33. Liu, M. H. et al. Adipose-derived stem cells were impaired in restricting CD4+T cell proliferation and polarization in type 2 diabetic ApoE^{-/-} mouse. *Mol. Immunol.* **87**, 152–160 (2017).
34. Aibar, S. et al. SCENIC: single-cell regulatory network inference and clustering. *Nat. Methods* **14**, 1083–1086 (2017).
35. Cristancho, A. G. & Lazar, M. A. Forming functional fat: a growing understanding of adipocyte differentiation. *Nat. Rev. Mol. Cell Biol.* **12**, 722–734 (2011).
36. Merrick, D. et al. Identification of a mesenchymal progenitor cell hierarchy in adipose tissue. *Science* **364**, eaav2501 (2019).
37. Kozhemyakina, E. et al. Identification of a Prg4-expressing articular cartilage progenitor cell population in mice. *Arthritis Rheumatol.* **67**, 1261–1273 (2015).
38. Yang, L. et al. Antioxidant metallothionein alleviates endoplasmic reticulum stress-induced myocardial apoptosis and contractile dysfunction. *Free Radic. Res.* **49**, 1187–1198 (2015).
39. Ruttkay-Nedecky, B. et al. The role of metallothionein in oxidative stress. *Int. J. Mol. Sci.* **14**, 6044–6066 (2013).
40. Emmert-Streib, F. & Glazko, G. V. Pathway analysis of expression data: deciphering functional building blocks of complex diseases. *PLoS Comput. Biol.* **7**, e1002053 (2011).
41. Reilly, C., Stewart, T. J., Renfrow, M. B. & Novak, J. Glycosylation in health and disease. *Nat. Rev. Nephrol.* **15**, 346–366 (2019).
42. Ioannidou, A., Goulielmaki, E. & Garinis, G. A. DNA damage: from chronic inflammation to age-related deterioration. *Front. Genet.* **7**, 187 (2016).
43. Iacono, G., Massoni-Badosa, R. & Heyn, H. Single-cell transcriptomics unveils gene regulatory network plasticity. *Genome Biol.* **20**, 1–20 (2019).
44. Squir, J. W. et al. Confronting false discoveries in single-cell differential expression. *Nat. Commun.* **12**, 5692 (2021).
45. Xiang, Q. et al. Transcriptome analysis and functional identification of adipose-derived mesenchymal stem cells in secondary lymphedema. *Gland Surg.* **9**, 558–574 (2020).
46. Lim, H. Y. et al. Hyaluronan receptor LYVE-1-expressing macrophages maintain arterial tone through hyaluronan-mediated regulation of smooth muscle cell collagen. *Immunity* **49**, 326–341.e7 (2018).
47. Varol, C., Mildner, A. & Jung, S. Macrophages: development and tissue specialization. *Annu. Rev. Immunol.* **33**, 643–675 (2015).
48. Jablonski, K. A. et al. Novel markers to delineate murine M1 and M2 macrophages. *PLoS ONE* **10**, e0145342 (2015).
49. Vandestienne, M. et al. TREM-1 orchestrates angiotensin II-induced monocyte trafficking and promotes experimental abdominal aortic aneurysm. *J. Clin. Invest.* **131**, e142468 (2021).
50. Joffre, J. et al. Genetic and pharmacological inhibition of TREM-1 limits the development of experimental atherosclerosis. *J. Am. Coll. Cardiol.* **68**, 2776–2793 (2016).
51. Efremova, M., Vento-Tormo, M., Teichmann, S. A. & Vento-Tormo, R. CellPhoneDB: inferring cell–cell communication from combined expression of multi-subunit ligand–receptor complexes. *Nat. Protoc.* **15**, 1484–1506 (2020).
52. Baer, P. C. Adipose-derived mesenchymal stromal/stem cells: an update on their phenotype in vivo and in vitro. *World J. Stem Cells* **6**, 256–265 (2014).
53. Hume, D. A. & MacDonald, K. P. A. Therapeutic applications of macrophage colony-stimulating factor-1 (CSF-1) and antagonists of CSF-1 receptor (CSF-1R) signaling. *Blood* **119**, 1810–1820 (2012).
54. Wang, Z., Kong, D., Li, Y. & Sarkar, F. PDGF-D signaling: a novel target in cancer therapy. *Curr. Drug Targets* **10**, 38–41 (2009).
55. Folestad, E., Kunath, A. & Wågsäter, D. PDGF-C and PDGF-D signaling in vascular diseases and animal models. *Mol. Asp. Med.* **62**, 1–11 (2018).
56. Hepler, C. et al. Identification of functionally distinct fibro-inflammatory and adipogenic stromal subpopulations in visceral adipose tissue of adult mice. *Elife* **7**, e39636 (2018).
57. Boufenzar, A. et al. Potentiation of NETs release is novel characteristic of TREM-1 activation and the pharmacological inhibition of TREM-1 could prevent from the deleterious consequences of NETs release in sepsis. *Cell Mol. Immunol.* **18**, 452–460 (2021).
58. Wolock, S. L., Lopez, R. & Klein, A. M. Scrublet: computational identification of cell doublets in single-cell transcriptomic data. *Cell Syst.* **8**, 281–291.e9 (2019).
59. Becht, E. et al. Dimensionality reduction for visualizing single-cell data using UMAP. *Nat. Biotechnol.* **37**, 38–44 (2019).
60. Bindea, G. et al. ClueGO: a cytoscape plug-in to decipher functionally grouped gene ontology and pathway annotation networks. *Bioinformatics* **25**, 1091–1093 (2009).
61. Subramanian, A. et al. Gene set enrichment analysis: a knowledge-based approach for interpreting genome-wide expression profiles. *Proc. Natl. Acad. Sci. USA* **102**, 15545–15550 (2005).
62. Liberzon, A. et al. The molecular signatures database hallmark gene set collection. *Cell Syst.* **1**, 417–425 (2015).
63. Chen, S., Zhou, Y., Chen, Y. & Gu, J. fastp: an ultra-fast all-in-one FASTQ pre-processor. *Bioinformatics* **34**, i884–i890 (2018).
64. Bray, N. L., Pimentel, H., Melsted, P. & Pachter, L. Near-optimal probabilistic RNA-seq quantification. *Nat. Biotechnol.* **34**, 525–527 (2016).
65. Pimentel, H., Bray, N. L., Puente, S., Melsted, P. & Pachter, L. Differential analysis of RNA-seq incorporating quantification uncertainty. *Nat. Methods* **14**, 687–690 (2017).